Journal of Alloys and Compounds 848 (2020) 156595

Contents lists available at ScienceDirect

Journal of Alloys and Compounds

journal homepage: http://www.elsevier.com/locate/jalcom

$Ni_{11\square}$ $(HPO_3)_8(OH)_6$ multifunctional materials: Electrodes for oxygen evolution reaction and potential visible-light active photocatalysts

Bogdan-Ovidiu Taranu , Madalina-Gabriela Ivanovici , Paula Svera , Paulina Vlazan ,
Paula Sfirloaga , Maria Poienar *

National Institute for Research and Development in Electrochemistry and Condensed Matter, Dr. A. P. Podeanu Street, No. 144, 300569, Timişoara, Romania

ARTICLE INFO

Article history:
Received 22 May 2020
Received in revised form
12 July 2020
Accepted 30 July 2020
Available online 3 August 2020

Keywords:
Nickel phosphite
Thermal stability
Structure
Oxygen evolution reaction
Photocatalyst

ABSTRACT

$Ni_{11\square}(HPO_3)_8(OH)_6$ nanorods were the focus of three different studies. First, the thermal behaviour of the material was investigated and it outlined a good thermal stability up to 400 °C. Second, a comparative electrochemical study concerning the OER performance in alkaline medium of several graphite electrodes modified with the nickel phosphite was performed. The most promising electrodes were further characterised electrochemically and the electrode modified with Nafion solution and 5 mg $Ni_{11\square}(HPO_3)_8(OH)_6$ exhibited the smallest overpotential value at the 10 mA cm^{-2} anodic current density (0.59 V), as well as the smallest Tafel slope (0.081 V dec^{-1}). Furthermore, the constant potential electrolysis test revealed that this electrode is fairly stable within a time span of 300 min. Third, the capacity of $Ni_{11\square}(HPO_3)_8(OH)_6$ nanorods to remove MB and RhB were investigated under simulated visible light irradiation and positive results were obtained for the application as visible-light active photocatalyst. All this together corroborated with the eco-friendly nature of the materials, reinforces the fact that the phosphite type compound is a promising candidate for the design of new multifunctional and advanced materials.

1. Introduction

In the last years, many efforts have been made in the study of phosphite transition metals corresponding to the $M_{11\square}(HPO_3)_8(OH)_6$ formula (with M = Ni, Co, Zn), first described in 1993 by Marcos et al. [1,2], for the implementation of these materials as electrodes for next generation supercapacitors [3–7] or as rechargeable cathode materials in aluminum ion batteries, for example [8]. These materials present high specific capacitance, rate capability and cycling properties and in order to improve their kinetic properties, composites with carbon materials -graphene and reduced graphene oxide (rGO) - have been designed [3–5,8]. In this context, different characteristic morphologies for nano/microstructured $Ni_{11\square}(HPO_3)_8(OH)_6$ samples have also been obtained (spheres, rods, microballs [9,10] and superstructures as hollow microspheres [5,9] or star-cross [11]) and their properties were carefully investigated, as it is known that this could play a key role in ions intercalation/extraction and electrolyte access, for example.

Today's scientific research into energy conversion and storage systems relies crucially on a few basic electrochemical reactions, as well as on the use of inexpensive highly active electrocatalyst materials intended to replace the costly noble metal catalysts [12–14]. Two of those reactions, the oxygen and hydrogen evolution reactions (OER and HER) take place during the water splitting process [15–17]. Unlike HER, OER is a slow, complex, four-electron transfer process [18,19] and great efforts have been made to synthesize catalysts that would allow it to take place at decreased overpotentials [12,20]. Nickel, for instance, an earth-abundant transition metal having a relatively low cost and great potential in water splitting [21,22], has been used intensively to synthesize electrocatalysts for OER, such as nickel oxides [23], hydroxides [24], sulfides [25], nitrides [26], phosphides [27] and phosphites [14], materials with performances that live up to the current demands of the water splitting field.

Herein, we present three different studies performed on the $Ni_{11\square}(HPO_3)_8(OH)_6$ material: an investigation of the thermal behaviour of $Ni_{11\square}(HPO_3)_8(OH)_6$ nanorods, a comparative electrochemical study involving 12 graphite electrodes modified with the

---

* Corresponding author. National Institute for Research and Development in Electrochemistry and Condensed Matter, Str. Dr. A. Păunescu Podeanu, nr.144, 300569, Timisoara, Romania.
E-mail address: maria_poienar@yahoo.com (M. Poienar).

https://doi.org/10.1016/j.jallcom.2020.156595
0925-8388/© 2020 Elsevier B.V. All rights reserved.

nickel phosphite that shows its ability to catalyse OER in alkaline medium and the photocatalytic activity of the compound under visible light irradiation on the degradation of methylene blue (MB) and rhodamine B (RhB) organic dyes. It should also be noted that following the remarkable results reported for $Ni_{11}\square(HPO_3)_8(OH)_6$ as a bifunctional overall water splitting electrocatalyst in Refs. [14], the electrochemical study described in the present paper was performed with a different electrode material, different suspensions containing the nickel phosphite for electrode modification and a different deposition method.

2. Experimental section

Synthesis of $Ni_{11}\square(HPO_3)_8(OH)_6$ materials was made by using high temperature and pressure hydrothermal synthesis as reported in Ref. [11].

The crystal structure has been visualized by the help of Vesta software [28].

The Raman spectra of the $Ni_{11}\square(HPO_3)_8(OH)_6$ sample was obtained using the MultiView-2000 system from Nanonics Imaging Ltd., Israel, equipped with a Shamrock 500i Spectrograph from ANDOR, United Kingdom. The analysis was performed at room temperature (RT) through a 10 × microscope objective, using a 514.5 nm laser wavelength as the excitation source with 30s exposure time.

TGA experiments were carried out by using a SETARAM apparatus, in which a typical 20–30 mg amount of sample was heated in air atmosphere at temperatures up to 800 °C.

Electrode preparation. Graphite tablets surface was modified by drop-casting 10 μL from suspensions with and without $Ni_{11}\square(HPO_3)_8(OH)_6$ powder. The suspensions were prepared using the following materials and reagents: $Ni_{11}\square$ $(HPO_3)_8(OH)_6$ powder, Nafion® 117 solution (Sigma-Aldrich), Graphene PureSheets Quattro (NanoIntegris) concentrated up to 0.6 mg mL^{-1} by centrifugation and redispersing, Carbon Black - Vulcan XC 72 (FuellCellStore), ethanol and isopropanol.

Twelve types of graphite-based modified electrodes were obtained by applying the suspensions on the graphite tablets and allowing them to dry for 24 h, in air, at RT. Table 1 shows the codes used to identify the unmodified electrode and each of the modified electrodes, together with the compositions of the suspensions used to modify the graphite tablets. The modified electrodes are denoted from G1 to G12 depending on the suspension used to modify them, while the unmodified graphite electrode is denoted G0.

Electrochemical experiments. The OER catalytic properties of $Ni_{11}\square$ $(HPO_3)_8(OH)_6$ were investigated electrochemically using a standard, single compartment, electrochemical glass cell equipped with three electrodes. The counter electrode was a Pt plate ($S = 0.8\ cm^2$), Ag/AgCl (saturated KCl) was used as reference and the modified graphite tablets together with an unmodified tablet were each used as the working electrode after insertion into an electrochemically inert support ($S = 0.07\ cm^2$). The electrodes were connected to a VoltaLab PGZ 402 Universal Potentiostat (Radiometer Analytical). The OER experiments and the double layer capacitance studies were performed in 0.1 mol L^{-1} KOH (pH = 13) aqueous electrolyte solution, while 1 mol L^{-1} KNO_3 solution containing 4 mmol L^{-1} $K_3[Fe(CN)_6]$ was used for electroactive surface area determinations. All experiments were carried out at RT. Linear sweep voltammetry (LSV) curves for OER measurements were recorded at a scan rate of 1 mV s^{-1}. The current densities (i) referred to in the text are geometrical current densities, unless otherwise specified. The measured potentials versus the reference electrode, performed with iR compensation, were converted to a reversible hydrogen electrode (RHE) scale (see Supplementary data).

Tafel slopes were calculated by plotting the overpotential values against the logarithm of the current density values obtained by taking into account the electroactive surface area of the electrodes, which was estimated using the Randles-Sevcik equation – (see Supplementary data). The same equation was also employed to estimate the diffusion coefficient of ferricyanide ions [29].

The photocatalytic experiments were performed using artificial light provided by a solar simulator (Sol2A 94042A, Oriel Instruments/Newport Corporation) and different types of organic dyes: RhB extra, MB for microscopy (Merck), and Methyl Orange-MO- (reagent Ph Eur) for $Ni_{11}\square$ $(HPO_3)_8(OH)_6$ material of varying amounts, 25 mg and 75 mg, respectively added in a glass vessel containing 25 ml dye aqueous solution of 2 mg L^{-1} concentration (see Supplementary data for detailed information).

Optical absorption spectra were recorded at RT on powder samples by a UV–Vis spectrometer Perkin Elmer type Lambda 950 with integrating sphere module in the 300–1000 nm range.

3. Results and discussion

3.1. Structural and thermal analysis of $Ni_{11}\square(HPO_3)_8(OH)_6$ materials

$Ni_{11}\square(HPO_3)_8(OH)_6$ materials crystallize within $P6_3mc$ space group and the unit cell parameters are *a* = 12.4589 (1) Å and *c* = 4.9543 (1) Å for the compound obtained as reported in Refs. [11], which will be investigated in this research study. The crystal structure is characterized by a 3D arrangement with NiO_6 octahedra forming two kinds of chains running along the *c* axis: smaller triangular ones occupied by 2/8 of the HPO_3 pseudotetrahedral

Table 1
The codes used to identify the unmodified electrode and each of the modified electrodes, together with the compositions of the suspensions used to modify the graphite tablets.

Electrode code	$Ni_{11}(HPO_3)_8(OH)_6$ powder [mg]	Nafion solution [μL]	rGO suspension [μL]	carbon black [mg]	Solution containing 80% ethanol, 15% water and 5% isopropanol [μL]
G0	-	-	-	-	-
G1	1	-	-	-	500
G2	5	-	-	-	500
G3	1	10	-	-	500
G4	5	10	-	-	500
G5	-	-	83	-	500
G6	-	-	-	10	500
G7	-	10	-	10	500
G8	-	10	83	-	500
G9	1	10	-	10	500
G10	5	10	-	10	500
G11	1	10	83	-	500
G12	5	10	83	-	500

groups and the larger ones with remaining three quarters of phosphite groups located on the walls (Fig. 1) [1,2,11]. These structural paths are of great importance for the intercalation of atoms, molecules or ions into the crystalline lattice and because of this, potential applications could be envisaged for the phosphite materials.

The morphology of the high pressure and temperature hydrothermally obtained $Ni_{11\square}(HPO_3)_8(OH)_6$ materials is characterised by the presence of rods shaped crystallites with a mean diameter of 50 nm and several micrometres length (Fig. 2) arranged also as spherical urchin-like superstructures within the compound [11].

Raman spectra of the nickel phosphite compound is reported. Raman scattering allows to determine one-phonon (transversal optical- TO- and longitudinal optical- LO- modes) and two-phonon (2TO, TO + LO, and 2LO modes) excitations along with one-, two- and four-magnon excitations [30,31]. For the $Ni_{11\square}(HPO_3)_8(OH)_6$ compound the following bands are observed in the Raman spectra: 380 cm^{-1}, 430 cm^{-1}, 474 cm^{-1}, 560 cm^{-1}, 620 cm^{-1}, 938 cm^{-1}, 1005 cm^{-1}, 1134 cm^{-1} and 1580 cm^{-1} as shown in Fig. 3. Taking into account the sample crystal structure and molecular formula, it is expected to see several specific Raman peaks, starting with the most prominent NiO bands. For $Ni_{11\square}(HPO_3)_8(OH)_6$, the peaks observed at 430 (TO), 560 (LO), 1005 (TO + LO) and 1580 cm^{-1} (two magnon excitation) are attributed to Ni—O vibrations in Ni^{2+} octahedral environment, the NiO bands around 500 and 1000 cm^{-1} being attributed to first order (1P) and second order (2P) phonon scattering, as it is reported in Ref. [32].

The Raman shift difference occurs because of size or strain/stress effects, highlighting the position and relative intensities of the three peaks which are in good agreement with the reported values of the NiO phase corresponding to first-order TO mode (496.5 cm^{-1}), LO mode (1093.1 cm^{-1}) and 2TOM (1524.8 cm^{-1}) phonon modes respectively [31].

The presence of the 1580 cm^{-1} lower band corresponds to the one of the O—H stretching vibration characteristic for the residual water, exchangeable OH^-, and deficient OH groups with a considerable amount of hydrogen bonding [33,34].

In addition, PO_3 symmetric and asymmetric deformations were detected at 620 cm^{-1} and 474 cm^{-1} respectively [35,36]. The band from 380 cm^{-1} may indicate the presence of $(PO_4)^{3-}$ ions [39] or PO_3 deformation and rocking modes, the POP deformations, together with the torsional and external modes that are found between 430 and 180 cm^{-1} [37].

The PO_3^- symmetric and asymmetric (degenerate) stretching vibration bands of the HPO_3^- are expected to be detected at 980 and 1100 cm^{-1} [33,38]. In the sample analysis, the two mentioned vibrations are observed with a slight shift at 938 and 1134 cm^{-1}, respectively. In order to do a better peak identification, due to the nearly localization and slightly shift of the NiO band in the Raman spectra and according to the studies from the literature [38], it was taken into account the fact that the first band characteristic for PO_3^- is sharp while the second one is broad.

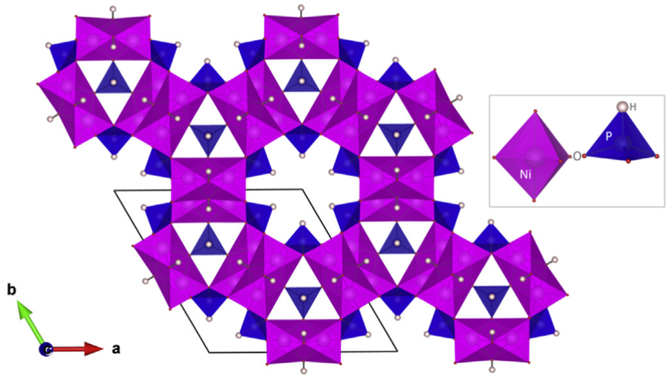

Fig. 1. Crystal structure of $Ni_{11\square}$ $(HPO_3)_8(OH)_6$ viewed along the [001] direction where two kinds of channels running along the *c* axis are observed (NiO_6 octaedra and HPO_3 structural unit are visualized separately at the right of the picture).

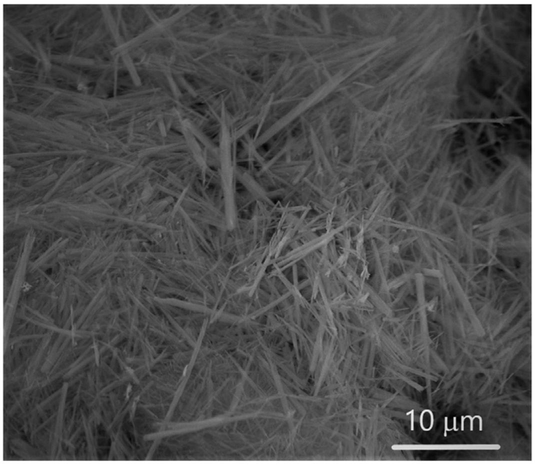

Fig. 2. SEM image of $Ni_{11\square}$ $(HPO_3)_8(OH)_6$ compound.

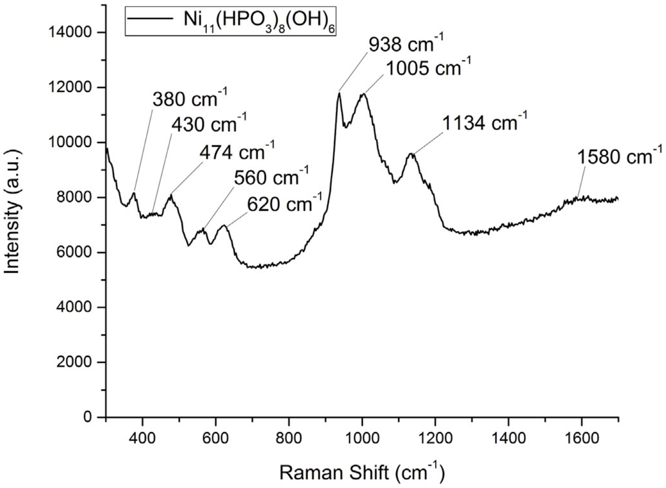

Fig. 3. Raman spectra of $Ni_{11\square}(HPO_3)_8(OH)_6$ at room temperature.

Thermal behaviour is also a very important aspect that has to be taken into consideration in order to use the materials for applications in different areas such as, for example, in electronics, catalysis or batteries. The thermogravimetric analysis for $Ni_{11\square}(HPO_3)_8(OH)_6$ in synthetic air atmosphere (Fig. 4) shows a decomposition process up to 800 °C. The first stage of mass loss occurs in the 45—400 °C range with a small mass loss of 0.4% of the sample weight, followed by the second important stage of weight loss up to 800 °C, with the total value of 6.8%. The sample recovered at 800 °C has a yellow colour and the X-Ray diffraction pattern indicates that it corresponds to the $Ni_3(PO_4)_2$ phase. The thermal stability of the studied material is therefore relatively high (up to approximately 400 °C), thus qualify the material to be used for applications in catalysis or batteries, for example.

3.2. Electrochemical properties of the as-prepared electrode

Fig. 5 shows the LSV curves obtained during OER studies performed on the 13 electrodes. Specifically, Fig. 5a presents the curves

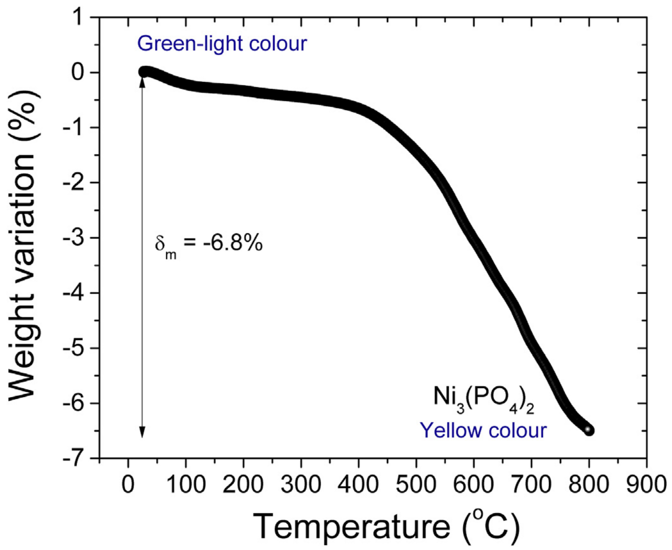

Fig. 4. Thermogravimetric analysis of $Ni_{11}\square(HPO_3)_8(OH)_6$ sample up to 800 °C in air atmosphere.

recorded on the G0 – G4, G6, G7, G9 and G10 electrodes, Fig. 5b presents the curves obtained on the G0 - G5, G8, G11 and G12 electrodes and Fig. 5c shows the curves corresponding to the 4 most electrocatalytically active modified electrodes (G2, G4, G10 and G12).

By analysing Fig. 5a and b it can be seen that most electrodes show poor electrocatalytic activity towards OER and only in 4 cases the geometrical current density observed during the recording of the LSV curves is higher than 5 mA cm^{-2}. The polarization curves recorded on these 4 modified electrodes (G2, G4, G10 and G12) are represented in Fig. 5c. The Ni^{2+}/Ni^{3+} oxidation peak [39,40] was difficult to observe when the polarization curves were recorded at $v = 1$ mV s^{-1}, but it became clear at higher values - as can be seen in the insert from Fig. 5c.

The 4 electrodes were further studied electrochemically in terms of the double-layer capacitance at the electrode/electrolyte solution interface and of their electroactive surface area. For these characterizations the potentials were recorded *vs.* the Ag/AgCl (sat. KCl) reference electrode.

The double layer capacitance at the electrode/electrolyte solution interface was determined using cyclic voltammetry. The voltammograms for the G2, G4, G10 and G12 modified electrodes were recorded in 0.1 mol L^{-1} KOH at various scan rates, in a potential range where no faradic currents were present ($-0.2 \div 0.2$ V). The current density values of the anodic and cathodic branches increased proportionally with those of the scan rate. The capacitive current density was calculated as the mean of the absolute values of anodic and cathodic current densities, selected at a potential where only double-layer adsorption and desorption features were present [41]. The double layer capacitance values for the 4 modified electrodes were obtained from the slope of the linear dependence of the capacitive current density (i_{dl}) *vs.* the scan rate (Fig. 6), and they are: 0.8572 mF cm^{-2} for G2, 1.0165 mF cm^{-2} for G4, 8.54 mF cm^{-2} for G10 and 0.5837 mF cm^{-2} for G12. A comparison between the values obtained for each electrode shows that the following double layer capacitance relationship exists between them: G12 < G2 < G4 < G10. It should also be pointed out that the linear increase of i_{dl} with the scan rate indicates the charging and discharging of the Helmholtz double layer [42].

For the G2, G4, G10 and G12 modified electrodes, the electroactive surface area (A) and diffusion coefficient of ferricyanide ions (D) were estimated at 298 K using the ferrous/ferric redox couple and the Randles Sevcik equation. Cyclic voltammograms were recorded at different scan rates (from 0.05 to 0.3 V s^{-1}) in 1 mol L^{-1} KNO_3 electrolyte solution containing 4 mmol L^{-1} $K_3[Fe(CN)_6]$. The curves obtained for G4 and G12 - the most electrocatalytically active electrodes - are exemplified in Fig. 7a and b and the results show that as the scan rate increases the current density values of

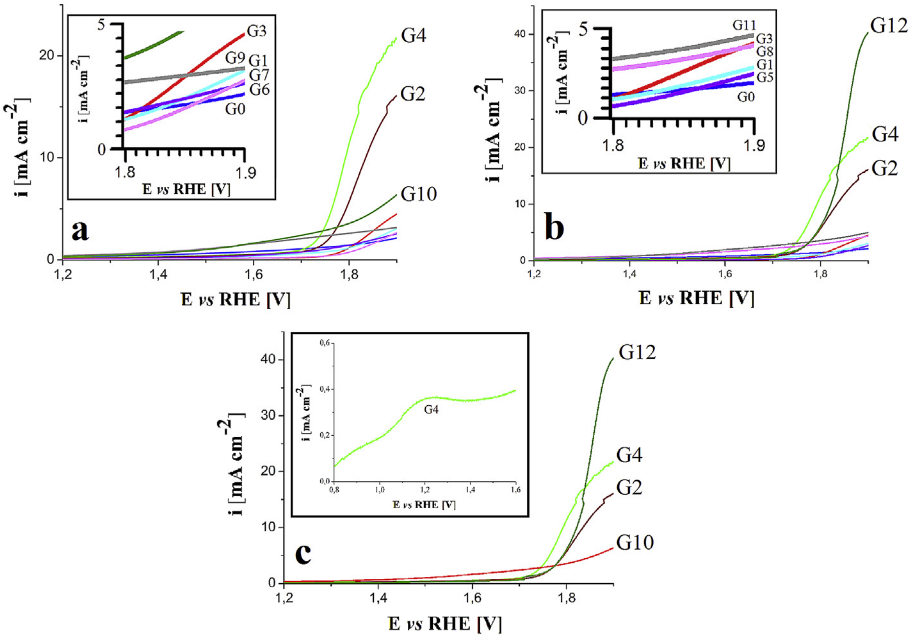

Fig. 5. iR-corrected OER polarization curves recorded on the G0 – G4, G6, G7, G9 and G10 electrodes (a), the G0 - G5, G8, G11 and G12 electrodes (b) and the G2, G4, G10 and G12 modified electrodes (c). Insets in (a) and (b) are intended for clarification purposes and show enlarged areas from the overlapped LSVs. Inset in (c) shows the Ni^{2+}/Ni^{3+} oxidation peak in case of the G4 electrode. Measurements were carried out in 0.1 mol L^{-1} KOH electrolyte solution, at a scan rate of 1 mV s^{-1}. Polarization curve from inset in (c) was recorded at 10 mV s^{-1} and is iR-uncorrected.

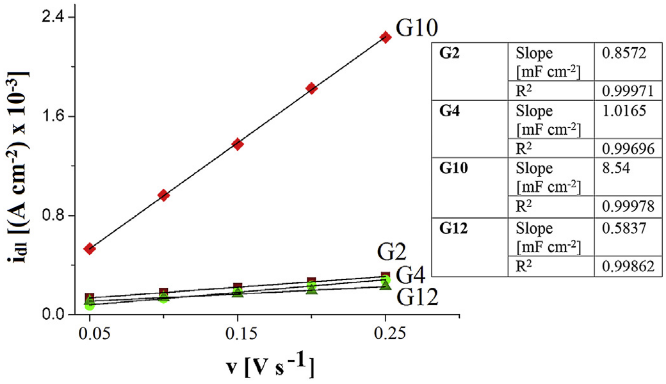

Fig. 6. Dependence of the capacitive current density on scan rate for the G2, G4, G10 and G12 modified electrodes. Experiments were performed in 0.1 mol L^{-1} KOH electrolyte solution, at $v = 0.05$, 0.1, 0.15, 0.2 and 0.25 V s^{-1}. The inserted table shows the slope and R^2 values calculated for each linear fit.

the anodic and cathodic peaks corresponding to the ferrous/ferric redox couple increase as well, which is an expected behaviour [43].

The obtained A and D values are presented in Table 2 and it can be seen that the G10 electrode has the highest electroactive surface area. In other words, even though this electrode's catalytic performance in the OER experiments was the poorest, the double layer capacitance and electroactive surface area are higher than those of the electrodes that were more catalytically active during the same experiments. It was expected that such an electrode would also have the best OER performance [44], but this isn't always the case. Thus, even though a modified electrode's OER activity is low, the materials used for modification can still provide it with a large electroactive surface area, high electronic conductivity and high electrolyte permeability [38].

The previously obtained double layer capacitance values, expressed in terms of the geometrical area of the modified electrodes, can now be expressed in terms of their electroactive surface area as well. The following values are obtained: 0.297 mF cm^{-2} for G2, 0.6776 mF cm^{-2} for G4, 1.8115 mF cm^{-2} for G10 and 0.3049 mF cm^{-2} for G12.

Fig. 7c shows the plot of the anodic and cathodic peak current densities *vs.* the square root of the scan rate for the G2, G4, G10 and G12 modified electrodes. The points represented on the plot correspond to the peak current densities of the oxidation and reduction peaks recorded in the presence of 4 mmol L^{-1} $K_3[Fe(CN)_6]$ in 1 mol L^{-1} KNO_3 electrolyte solution, at $v = 0.05$, 0.1, 0.15, 0.2, 0.25 and 0.3 V s^{-1}. The redox peak currents are proportional to the square root of the scan rate indicating a diffusion controlled electron-transfer process [43].

The LSV curves recorded on the G2, G4, G10 and G12 modified electrodes during the OER experiments are presented in Fig. 8a. The current density values take into account the estimated electroactive surface area of the electrodes and it can be seen that of the 4 modified electrodes the G4 electrode has the best OER electrocatalytic properties up to i ≈ 12.25 mA cm^{-2}, at which point its polarization curve intersects that of the G12 electrode (E ≈ 1.85 V *vs.* RHE). At higher current densities the G12 electrode is the most electrocatalytically active. In case of the LSV curves recorded on the G4 and G12 electrodes, the difference between the potential values corresponding to $i = 5$ mA cm^{-2} is $E_{G12} - E_{G4} = 0.04$ V *vs.* RHE and for $i = 10$ mA cm^{-2} the same difference becomes 0.024 V *vs.* RHE. After the two LSV curves intersect they begin to move away from each other and at $i = 14.5$ mA cm^{-2} the potential difference $E_{G4} - E_{G12} = 0.039$ V *vs.* RHE.

Compounds with electrocatalytic properties towards OER are often used in combinations with carbon based materials, such as rGO and carbon black [45,46], because of their ability to enhance the conductivity of these compounds. However, experimental conditions can lead to the oxidation of the carbon based materials which in turn has a negative effect on the catalyst's activity [47]. We suspect this is the reason why the carbon black containing modified electrode (G10) had the poorest performance during the OER experiments out of the 4 selected electrodes and it may also be why the rGO containing modified electrode (G12) didn't perform better than the G4 electrode at low current densities.

In order to study the catalytic kinetics of the 4 OER activity exhibiting electrodes, Tafel curves were obtained for each of them (Fig. 8b) and the linear regions of these curves were fitted to the Tafel equation: $\eta = b \times \log(i) + a$, where η is the overpotential, i is the current density (which in this case is based on the estimated electroactive surface area) and b is the Tafel slope. The Tafel slope of the G4 electrode has the lowest value (0.081 V dec^{-1}) and is followed by the slope values of the G12, G2 and G10 electrodes. These results indicate that the G4 modified electrode presents more rapid OER kinetics and superior activity [48].

Since stability is an important parameter in the study of the OER activity of electrocatalysts [48], the chronoamperometric (CA) response of the G4 modified electrode was recorded while

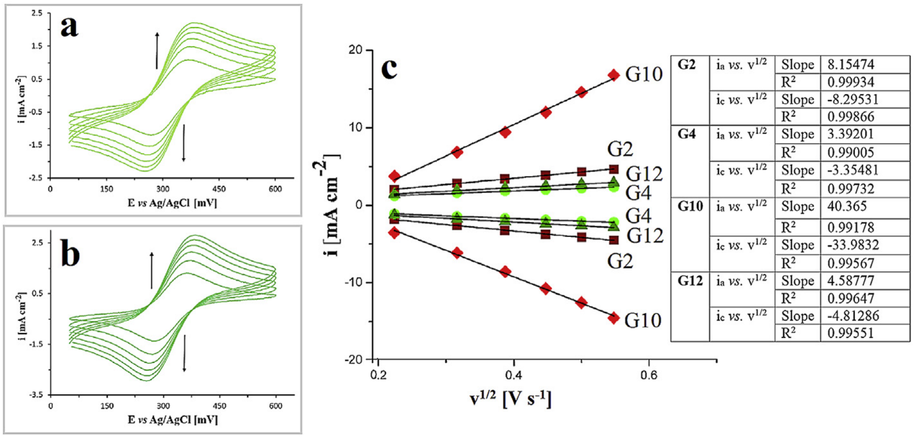

Fig. 7. Cyclic voltammograms recorded on the G4 (a) and G12 (b) modified electrodes. The plot of the anodic and cathodic peak current densities *vs.* the square root of scan rate for the G2, G4, G10 and G12 modified electrodes (c). Experiments were performed in 1 mol L^{-1} KNO_3 electrolyte solution containing 4 mmol L^{-1} $K_3[Fe(CN)_6]$, at $v = 0.05$, 0.1, 0.15, 0.2, 0.25 and 0.3 V s^{-1}. The inserted table shows the slope and R^2 values obtained for each linear fit.

Table 2
The estimated values of the electroactive surface area (A) and of the ferricyanide ions diffusion coefficient (D) in case of the G2, G4, G10 and G12 modified electrodes.

Electrode		
G2	A [cm^2]	0.202
	D [$cm^2\ s^{-1}$]	5.571×10^{-5}
G4	A [cm^2]	0.105
	D [$cm^2\ s^{-1}$]	1.518×10^{-5}
G10	A [cm^2]	0.33
	D [$cm^2\ s^{-1}$]	1.51×10^{-4}
G12	A [cm^2]	0.134
	D [$cm^2\ s^{-1}$]	2.46×10^{-5}

maintaining constant for 5 h the overpotential of 0.59 V, required to achieve the benchmarking current density of 10 mA cm^{-2} [49]. The obtained time-dependent current density curve is presented Fig. 8c and it shows that the electrode is fairly stable. The current density slightly increases until reaching a value of 10.33 mA cm^{-2} at t ≈ 31 min (an increase of 3.3%) and then it begins to slowly decrease, reaching the lowest value of 9.57 mA cm^{-2} at t = 300 min (a 4.3% decrease).

The LSVs recorded before and after CA measurements on the G4 electrode (denoted G4 and G4') are represented in the inset from Fig. 8c. The two polarization curves were obtained in the same conditions (0.1 mol L^{-1} KOH with a scan rate of 1 mV s^{-1}) and a comparison between them indicates that the CA experiment led to a small decrease in overpotential of 0.02 V, at the current density of 10 mA cm^{-2}. This result supports the claim that the graphite electrode modified with Nafion and 5 mg $Ni_{11\square}(HPO_3)_8(OH)_6$ is fairly stable.

A comparison between the results of the present OER study and those obtained by Menezez et al. [14] outlines the fact that while the value of the Tafel slope calculated for the G4 modified electrode is slightly lower, 81 mV dec^{-1} *vs.* 91 mV dec^{-1}, the overall electrocatalytic performance of the best electrode manufactured by the latter is superior. However, it has been shown, for instance, that by increasing the concentration of the KOH electrolyte solution from 0.1 mol L^{-1} to 1 mol L^{-1} the catalyst will exhibit a higher current density and a decrease in the overpotential corresponding to the current density values [50]. Future studies will focus on the modification of this parameter and will discuss its effect on the experimental results.

Studies performed on OER electrocatalysts with a structure similar to that of $Ni_{11\square}(HPO_3)_8(OH)_6$ have been reported in the scientific literature and in one such study [51], undoped and Fe-doped $Co_{11}(HPO_3)_8(OH)_6$ nanosheets arrays were fabricated on Ni foam and evaluated in terms of their catalytic activity towards OER and HER processes. For OER, in 1 mol L^{-1} KOH solution, the overpotential value attained at 20 mA cm^{-2} and the Tafel slope value were 311 mV and 78.2 mV dec^{-1} in case of the undoped material, while for the Fe-doped compound they were 206 mV and 47 mV dec^{-1}. Comparing these values with those obtained in our study and those published by Menezez et al., it is quite clear that the Fe-doped $Co_{11}(HPO_3)_8(OH)_6$ has better electrocatalytic properties. Still, the experiments performed by Menezez et al. with $Ni_{11\square}(HPO_3)_8(OH)_6$ on Ni foam in 1 mol L^{-1} KOH solution revealed an overpotential value of 232 mV (attained at 10 mA cm^{-2}) and the previously mentioned Tafel slope value of 91 mV dec^{-1}. These values place nickel phosphite among the very promising materials for energy conversion and storage applications, a conclusion supported by the comparative literature study performed by Menezez et al. which shows that the 232 mV OER overpotential is much lower than those of noble catalysts and one of the lowest in comparison to recently reported OER catalysts [14].

As for the electrochemical study described in this paper, its aim was to identify new combinations containing $Ni_{11\square}(HPO_3)_8(OH)_6$ that can catalyse OER in alkaline medium and thus increase the knowledge regarding electrodes modified with such combinations.

The electrocatalytic performance for the OER of the composition containing $Ni_{11\square}(HPO_3)_8(OH)_6$ and Nafion, applied on graphite

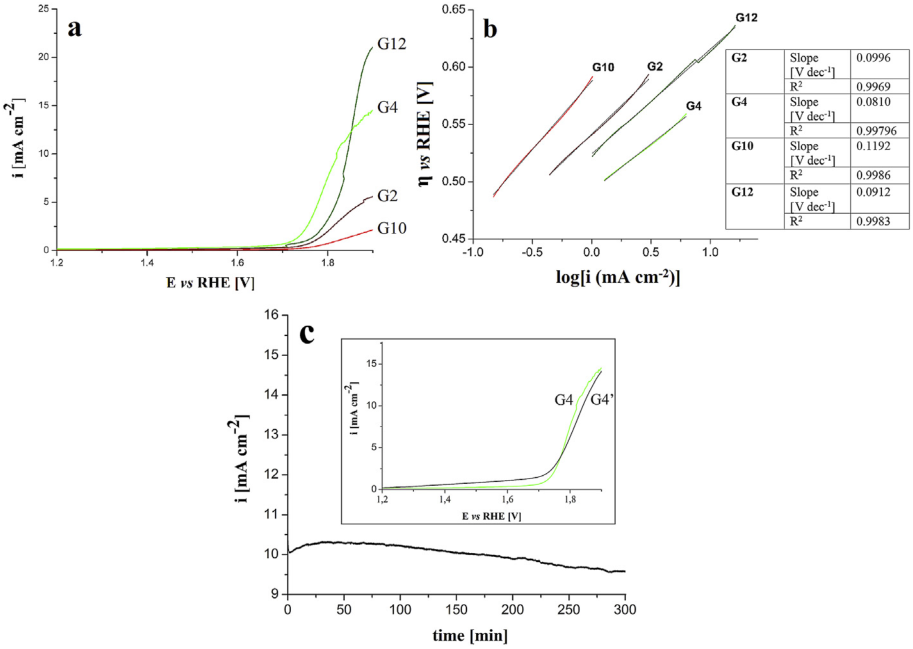

Fig. 8. iR-corrected OER polarization curves recorded on the G2, G4, G10 and G12 modified electrodes (a); The Tafel curves of the G2, G4, G10 and G12 modified electrodes and inserted table showing the Tafel slopes and R^2 values (b); CA responses of the G4 modified electrode in OER conditions at an overpotential corresponding to i = 10 mA cm^{-2} and inset showing the LSV recorded on the G4 electrode overlapped with the one obtained on the same electrode but after the CA experiment (c). All experiments were performed in 0.1 mol L^{-1} KOH.

substrate, and that of other electrocatalysts reported in the scientific literature, in 0.1 mol L^{-1} KOH electrolyte solution, is presented in Table S1 (see Supplementary data). The survey of the scientific literature from the past 10 years reveals the following: in terms of overpotential, the value obtained in our study for the G4 modified electrode is among the highest values reported in the literature and in terms of Tafel slope, Table S1 lists 21 values from various published studies, 12 of which are higher than the value obtained for the G4 electrode, while the remaining 9 are lower.

3.3. *Photocatalytic performance*

The organic dyes tested in the evaluation of the $Ni_{11\square}(HPO_3)_8(OH)_6$ nanorods photocatalytic properties may be classified in two types from the point of view of their molecular charge upon dissociation in aqueous based solution: cationic (RhB and MB) and anionic (MO) [52].

In the first stage, the experiments were carried out using 25 mg catalyst and 25 ml of aqueous dye solution with 2 mg L^{-1} initial concentration. The first set of results represented in Fig. 9a illustrates that for the given operating conditions, the catalyst has no photocatalytic action for MO degradation. In contrast with the MO experiment, a slight concentration decrease for RhB aqueous solution could be noticed and an even more prominent decrease for the MB aqueous solution. These results can be correlated with numerous experimental and mechanism studies of the photocatalytic process reported in the literature, where the cationic dyes may be more efficiently degraded than the anionic dyes by the oxidative species, mainly the hydroxyl radicals, $\cdot OH$ and the superoxide radical anions, $\cdot O_2^-$, derived from the photoexcited electrons and holes, respectively. Moreover, the nonexistent adsorption of MO on the catalyst could contribute, as well, to the lacking photocatalytic activity [47,52–56].

In order to identity the particular catalyst action for RhB and MB removal occurred as a result of both the adsorption-desorption and photodegradation processes, additional photocatalytic experiments were performed by varying the amount of the $Ni_{11\square}(HPO_3)_8(OH)_6$ material. Fig. 9b shows that the concentration of RhB aqueous solution at the end of the experiments decreased as the amount of added catalyst increased. Thus, in the absence of the catalyst, RhB does not degrade during the photocatalytic experiment, which means that photolysis of RhB does not occur in this media. Adding 25 mg catalyst led to the reduction of RhB aqueous solution concentration (approximately 6.3%) at the end of the experiment, wherein 2.6% resulted during the adsorption-desorption stage. Increasing the catalyst amount to 75 mg, the removal of the RhB reached 14%, from which 6.2% represents the effect of adsorption-desorption process. In these conditions, the contribution of 25 mg and 75 mg of $Ni_{11\square}(HPO_3)_8(OH)_6$ nanoparticles in the photocatalytic degradation of RhB is 3.7% and 7.8%, respectively. The visual decolorization of the RhB solution is hardly detected for the experiments conducted with 25 mg and 75 mg catalyst (Fig. 10).

Contrary to RhB, MB shows a significant degradation during the photolysis process, as the MB concentration decreased up to 49.4%, of which around 8% is obtained in the adsorption stage. In comparison with the photolysis experiment, the addition of 25 mg catalyst had almost no effect on improving the MB removal in the adsorption-desorption, but led to a higher MB degradation (of 53%) after solar light irradiation. In this case, as shown in Fig. 10, the decolorization of the MB solution after adsorption and visible light irradiation is more visible. Therefore, the difference of 3.6% in the photodegradation efficiency is given by the photocatalytic activity of the 25 mg catalyst. A more obvious increase of MB adsorption was obtained by increasing the catalyst dosage to 75 mg, whereas the photodegradation of MB was dramatically reduced to a value below 49.4% obtained in the photolysis process. According to other photocatalytic studies, the inhibition of photocatalytic degradation may appear as a consequence of dye solution turbidity caused by an excessive amount of catalyst which further blocks the light penetration in the suspension and slows the degradation rate [56–58]. These positive results, more clearly revealed in the photocatalytic experiments carried out with RhB, prove the potential application of $Ni_{11\square}(HPO_3)_8(OH)_6$ as a visible-light active photocatalyst.

To the best of our knowledge, there is only one study reported in the literature that investigated the photocatalytic properties of the $Ni_{11\square}(HPO_3)_8(OH)_6$ compound [10]. In this study, the capacity of wax-berry like $Ni_{11\square}(HPO_3)_8(OH)_6$ microballs to remove MB and RhB were investigated under both UV and visible light irradiation, wherein the experiments conducted under the visible light irradiation showed that $Ni_{11\square}(HPO_3)_8(OH)_6$ microballs have almost no photocatalytic activity (0.4% for MB and 0.3% for RhB) after 100 min of visible light exposure. The best results were obtained under UV light wherein the degradation of MB and RhB by the as-synthetized catalyst were 35.5% and 8.2% after 90 min irradiation.

The optical properties of the material from this study were investigated using UV–Vis spectroscopy. The insert in Fig. 11 illustrates that the absorption spectrum in the visible-light domain of the $Ni_{11\square}(HPO_3)_8(OH)_6$ nanorods displays a maximum absorption peak at 522 nm and two other smaller peaks at 388 and 602 nm.

The optical band gap energy (E_g) value was calculated from the diffuse reflectance spectrum using the Kubelka-Munk equation: $F(R) = (1\text{-}R)^2/2R = \alpha/S$, where α is the absorption coefficient, S is the scattering coefficient (which is practically wavelength independent when the particle size is larger than 5 μm) and R is the reflectance [60]. The calculated direct band gap ($E_g = 2.6$ eV)- Fig. 11- corresponds with the absorption in the visible-light spectrum, as pointed out in Ref. [61], which could explain the photocatalytic activity of $Ni_{11\square}(HPO_3)_8(OH)_6$ particles under solar light irradiation,.

In [10], the $Ni_{11\square}$ $(HPO_3)_8(OH)_6$ microballs present a maximum absorption peak at 413 nm and two other at 683 and 766 nm, thus different from our study and may be related to the different morphology (nanorods in our case and microballs in Ref. [10]). A morphology dependence of the UV–Vis absorption spectrum was also observed for $Co_{11}(HPO_3)_8(OH)_6$ microparticles and nanowires: the lambda onset recorded from the nanowire sample is about 255 nm and that from the microparticle sample is about 340 nm [62]. Thus, a 85 nm blue shift was observed in the spectrum from the nanowire sample which was explained based on the quantum confinement model [63,64].

Developing new materials as visible-light active photocatalysts has gained a lot of interest due to the necessity to extend the application of photocatalysts towards an enhanced exploitation of the solar light energy. For this reason, numerous studies were conducted to investigate the photocatalytic activities of different materials with absorption response to longer wavelengths (>400 nm). Among the representative visible light driven photocatalyst reported in the literature for degradation of the organic dyes, there may be mentioned materials based on C_3N_4, WO_3, TiO_2, Ag_3PO_4, $BiVO_4$. Still, due to variety of factors affecting the organic dyes degradation by photocatalysis (pH, type of the dye and respectively of the photocatalyst, the intensity of radiation, photocatalyst concentration, dye loading) and different conditions selected for the experimental studies, it is very difficult to make an appropriate and comprehensive comparison between photocatalytic activities of various materials [61]. However, in Table 2S (see Supplementary data), the photocatalytic efficiencies of several aforementioned visible light active materials, determined in

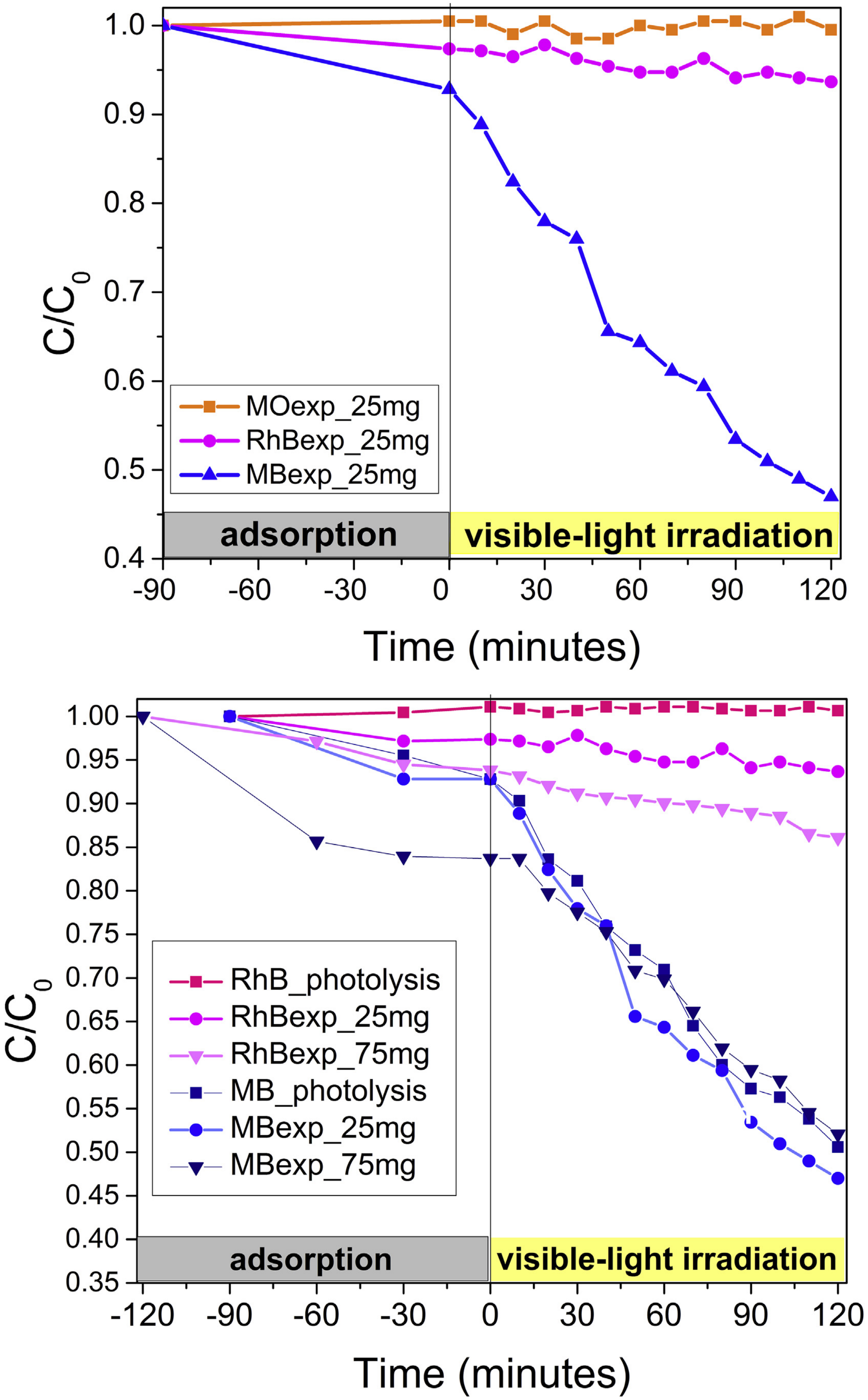

Fig. 9. Photocatalytic tests using 25 mg catalyst and 25 ml aqueous dye solution (MO, RhB, and MB) of 2 mg L^{-1} initial concentration (a); Photocatalytic tests using 25 ml aqueous dye solution (RhB and MB) of 2 mg L^{-1} initial concentration and different amount of catalyst (with no catalyst, 25 mg and 75 mg catalyst) (b).

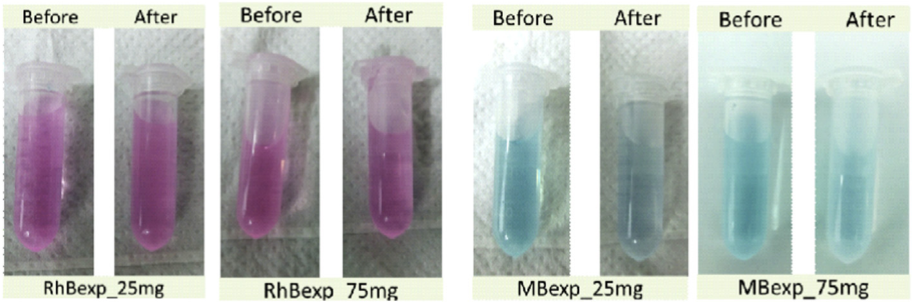

Fig. 10. Images of RhB and MB solution samples before and after photocatalytic experiment for 25 and 75 mg catalyst, respectively.

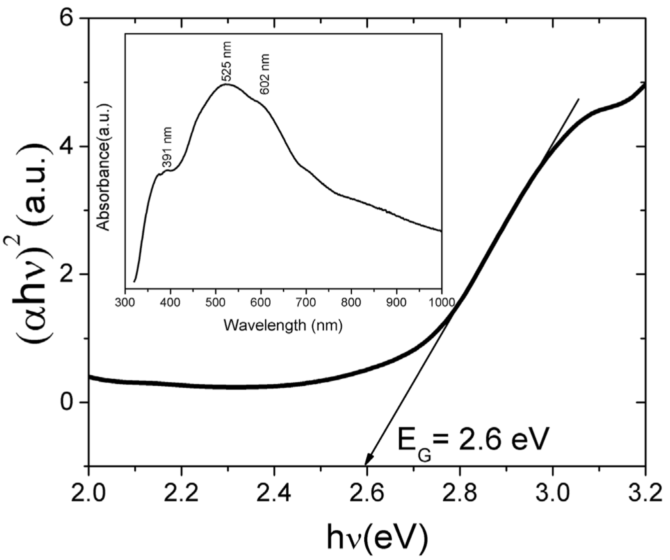

Fig. 11. Calculated band gap energy of $Ni_{11\square}(HPO_3)_8(OH)_6$ compound, insert: UV–Visible absorption spectrum in the 300–1000 nm range.

various studies using particular experimental conditions for elimination of MB and RhB from aqueous dyes solution are presented, along with our results on Ni compound.

In the present study, only 14% of RhB and around 53% of MB were removed from the aqueous solution using a catalyst concentration of 3 g L^{-1} and respectively 1 g L^{-1}, 25 ml of dye solution with initial concentration of 2 mg L^{-1} after 2 h of artificial solar radiation. These results are quite inferior in comparison with the results of other studies presented above considering that smaller volumes, lower concentration of aqueous dyes solutions and the same or even higher catalyst concentration were involved in the present research. However, the degradation of RhB under solar irradiation caused exclusively by the addition of the $Ni_{11\square}(HPO_3)_8(OH)_6$ proved the photocatalytic potential of the material.

FT-IR and Raman experiments were performed in order to investigate the stability of the $Ni_{11\square}(HPO_3)_8(OH)_6$ materials after the electrochemical and photocatalysis experiments. The measurements are presented in the supplementary data file and the study show that the materials are stable after the reactions.

4. Conclusions

Electrochemical experimental results show that $Ni_{11\square}(HPO_3)_8(OH)_6$ acts as OER catalyst in alkaline medium and that, out of the 12 investigated modified electrodes, the G4 electrode - obtained by applying a composition containing 10 μL Nafion solution and 5 mg $Ni_{11\square}(HPO_3)_8(OH)_6$ on graphite substrate - has more rapid OER kinetics and superior electrocatalytic activity. Our work contributes to the increase of the knowledge regarding electrodes modified with combinations containing nickel phosphite, a material that has already been shown, via the work of Menezez et al. [14], to have a place among the very promising materials for the development of new devices for energy conversion and storage through water splitting, that are of great interest in light of today's energy crisis and environmental issues.

Further OER catalysis studies on $Ni_{11\square}(HPO_3)_8(OH)_6$ involving an increase in the concentration of the alkaline electrolyte solution, as well as the presence of the combined effects of carbon black and rGO are underway. In addition, interesting results were obtained for the photocatalytic activity of the nickel phosphite that has been tested for removal of RhB and MB under visibile light irradiation.

CRediT authorship contribution statement

Bogdan-Ovidiu Taranu: Formal analysis, Writing - original draft, Investigation, Writing - review & editing. **Madalina-Gabriela Ivanovici:** Formal analysis, Investigation, Writing - review & editing. **Paula Svera:** Formal analysis, Investigation, Writing - review & editing. **Paulina Vlazan:** Formal analysis, Investigation, Supervision. **Paula Sfirloaga:** Formal analysis, Investigation, Validation. **Maria Poienar:** Conceptualization, Writing - review & editing, Supervision, Project administration, Funding acquisition, Formal analysis.

Declaration of competing interest

The authors declare that they have no known competing financial interests or personal relationships that could have appeared to influence the work reported in this paper.

Acknowledgements

M.P. acknowledges financial support for this work provided by the joint French-Romanian project ANR-UEFISCDI, contracts no. 8 RO-Fr/01.01.2013, code PN-II-ID-JRP-2011-2-0056, COFeIn. M. G. I. acknowledges financial support for this work provided by the CIA_CLIM - Smart buildings/ PN-III-P1-1.2-PCCDI-2017-0391 adaptable to the climate change effects, granted by Romanian Ministry of Research and Innovation, CCCDI–UEFISCDI. The authors thank Dr Radu Bănică for fruitful discussions and Dr Anamaria Dabici for UV-Vis measurements.

Appendix A. Supplementary data

Supplementary data to this article can be found online at https://doi.org/10.1016/j.jallcom.2020.156595.

References

[1] M.D. Marcos, P. Amoros, A. Le Bail, Synthesis and crystal structure of a tubular hydroxyphosphite: $Zn_{11}(HPO_3)_8(OH)_6$, J. Solid State Chem. 107 (1993) 250–257.

[2] M.D. Marcos, P. Amoros, A. Beltran-Porter, R. Martinez-Manez, J.P. Attfield, Novel crystalline microporous transition-metal phosphites $M_{11}(HPO_3)_8(OH)_6$ (M = Zn, Co, Ni). X-ray powder diffraction structure determination of the cobalt and nickel derivatives, Chem. Mater. 5 (1993) 121–128.

[3] H. Pang, C. Wei, Y. Ma, S. Zhao, G. Li, J. Zhang, J. Chen, S. Li, Nickel phosphite superstructures assembled by nanotubes: original application for effective electrode materials of supercapacitors, Chem. Plus. Chem. 78 (2013) 546–553.

[4] Y. Gao, J. Zhao, Z. Run, G. Zhang, H. Pang, Microporous $Ni_{11}(HPO_3)_8(OH)_6$ nanocrystals for high-performance flexible asymmetric all solid-state supercapacitors, Dalton Trans. 43 (2014) 17000–17005.

[5] D. Zhang, Y. Zhang, Y. Luo, Y. Zhang, X. Li, X. Yu, H. Ding, P. Chu, L. Sun, High-performance asymmetrical supercapacitor composed of rGO-enveloped nickel phosphite hollow spheres and N/S co-doped rGO aerogel, Nano Res. 11 (2018) 1651–1663.

[6] B. Li, Y. Shi, K. Huang, M. Zhao, J. Qiu, H. Xue, H. Pang, Cobalt-doped nickel phosphite for high performance of electrochemical energy storage, Small 14 (2018) 1703811.

[7] H. Pang, Z. Yan, Y. Wei, X. Li, J. Li, L. Zhang, J. Chen, J. Zhang, H. Zheng, The morphology evolution of nickel phosphite hexagonal polyhedrons and their primary electrochemical capacitor applications, Part. Part. Syst. Char. 30 (2013) 287–295.

[8] J. Tu, H. lei, M. Wang, Z. Yu, S. Jiao, Facile synthesis of $Ni_{11}(HPO_3)_8(OH)_6$/rGO nanorods with enhanced electrochemical performance for aluminum-ion batteries, Nanoscale 10 (2018) 21284–21291.

[9] Z. Gu, T. Zhai, B. Gao, G. Zhang, D. Ke, Y. Ma, J. Yao, Controlled hydrothermal synthesis of nickel phosphite nanocrystals with hierarchical superstructures, Cryst. Growth Des. 7 (2007) 825–830.

[10] Y. Zhang, Z. Peng, X. Fu, Controlled synthesis and photocatalytic performance of waxberry-like $Ni_{11}(HPO_3)_8(OH)_6$ microballs, J. Mater. Res. 32 (2017) 2819–2828.

[11] M. Poienar, A. Maignan, P. Sfirloaga, S. Malo, P. Vlazan, A. Guesdon, F. Lainé, J. Rouquette, C. Martin, Polar space group and complex magnetism in $Ni_{11\square}(HPO_3)_8(OH)_6$: towards a new multiferroic material? Solid State Sci. 39 (2015) 92–96.

[12] I. Concina, Z.H. Ibupoto, A. Vomiero, Semiconducting metal oxide nanostructures for water splitting and photovoltaics, Adv. Energy Mater. 7 (2017) 1700706.

[13] M. Chhetri, S. Sultan, C.N.R. Rao, Electrocatalytic hydrogen evolution reaction activity comparable to platinum exhibited by the Ni/Ni$(OH)_2$/graphite electrode, Proc. Natl. Acad. Sci. Unit. States Am. 114 (2017) 8986–8990.

[14] P.W. Menezes, C. Panda, S. Loos, F. Bunschei-Bruns, C. Walter, M. Schwarze, X. Deng, H. Dau, M. Driess, A structurally versatile nickel phosphite acting as a robust bifunctional electrocatalyst for overall water splitting, Energy Environ. Sci. 11 (2018) 1287–1298.

[15] S. Deng, F. Yang, Q. Zhang, Y. Zhong, Y. Zeng, S. Lin, X. Wang, X. Lu, C.Z. Wang, L. Gu, X. Xia, J. Tu, Phase modulation of (1T-2H)-$MoSe_2$/TiC-C shell/core arrays via nitrogen doping for highly efficient hydrogen evolution reaction, Adv. Mater. 30 (2018) 1802223.

[16] J. Li, G. Du, X. Cheng, P. Feng, X. Luo, CoNiP/NC polyhedrons derived from cobalt-based zeolitic imidazolate frameworks as an active electrocatalyst for oxygen evolution, Chin. J. Catal. 39 (2018) 982–987.

[17] R. Souleymen, Z. Wang, C. Qiao, M. Naveed, C. Cao, Microwave-assisted synthesis of graphene-like cobalt sulfide freestanding sheets as an efficient bifunctional electrocatalyst for overall water splitting, J. Mater. Chem. A 6 (2018) 7592–7607.

[18] B. Pierozynski, T. Mikolajczyk, M. Luba, A. Zolfaghari, Kinetics of oxygen evolution reaction on nickel foam and platinum-modified nickel foam materials in alkaline solution, J. Electroanal. Chem. 847 (2019) 113194.

[19] R.L. Doyle, M.E.G. Lyons, An electrochemical impedance study of the oxygen evolution reaction at hydrous iron oxide in base, Phys. Chem. Chem. Phys. 15 (2013) 5224–5237.

[20] S.K. Ghosh, H. Rahaman, Chapter 16: noble metal–manganese oxide hybrid nanocatalysts, in: S. Mohapatra, T.A. Nguyen, P. Nguyen-Tri (Eds.), Noble Metal-Metal Oxide Hybrid Nanoparticles. Fundamentals and Applications. Micro and Nano Technologies, vol. 313, Woodhead Publishing, 2019, ISBN 978-0-12-814134-2, p. 340.

[21] R. Subbaraman, D. Tripkovic, K.-C. Chang, D. Strmcnik, A.P. Paulikas, P. Hirunsit, M. Chan, J. Greeley, V. Stamenkovic, N.M. Markovic, Trends in activity for the water electrolyser reactions on 3d M(Ni,Co,Fe,Mn) hydr(oxy) oxide catalysts, Nat. Mater. 11 (2012) 550–557.

[22] L. Han, S. Dong, E. Wang, Transition-metal (Co, Ni, and Fe)-based electrocatalysts for the water oxidation reaction, Adv. Mater. 28 (2016) 9266–9291.

[23] I.J. Godwin, M.E.G. Lyons, Enhanced oxygen evolution at hydrous nickel oxide electrodes via electrochemical ageing in alkaline solution, Electrochem. Commun. 32 (2013) 39–42.

[24] M. Gao, W. Sheng, Z. Zhuang, Q. Fang, S. Gu, J. Jiang, Y. Yan, Efficient water oxidation using nanostructured α-nickel-hydroxide as an electrocatalyst, J. Am. Chem. Soc. 136 (2014) 7077–7084.

[25] W. Zhou, X.-J. Wu, X. Cao, X. Huang, C. Tan, J. Tian, H. Liu, J. Wang, H. Zhang, Ni_3S_2nanorods/Ni foam composite electrode with low overpotential for electrocatalytic oxygen evolution, Energy Environ. Sci. 6 (2013) 2921–2924.

[26] M. Shalom, D. Ressnig, X. Yang, G. Clavel, T.P. Fellinger, M. Antonietti, Nickel nitride as an efficient electrocatalyst for water splitting, J. Mater. Chem. A 3 (2015) 8171–8177.

[27] B. You, N. Jiang, M. Sheng, M.W. Bhushan, Y. Sun, Hierarchically Porous Urchin-like Ni_2P superstructures supported on nickel foam as efficient bifunctional electrocatalysts for overall water splitting, ACS Catal. 6 (2016) 714–721.

[28] K. Momma, F. Izumi, VESTA 3 for three-dimensional visualization of crystal, volumetric and morphology data, J. Appl. Crystallogr. 44 (2011) 1272–1276.

[29] A. Baciu, A. Remes, E. Ilinoiu, F. Manea, S.J. Picken, J. Schoonman, Carbon nanotubes composite for environmentally friendly sensing, Environ. Eng. Manag. J. 11 (2012) 239–246.

[30] N. Mironova-Ulmane, A. Kuzmin, I. Sildos, M. Pärs, Polarisation dependent Raman study of single-crystal nickel oxide, Cent. Eur. J. Phys. 9 (2011) 1096–1099.

[31] T. Thema, E. Manikandan, A. Gurib-Fakim, M. Maaza, Single phase Bunsenite NiO nanoparticles green synthesis, J. Alloys Compd. 657 (2016) 655–661.

[32] Z. Qiu, D. He, Y. Wang, X. Zhao, W. Zhao, H. Wu, High performance asymmetric supercapacitors with ultrahigh energy density based on hierarchical carbon nanotubes@NiO core–shell nanosheets and defect-introduced graphene sheets with hole structure, RSC Adv. 7 (2017) 7843–7856.

[33] Y.Y. Tong, C.D. Gu, J.L. Zhang, M.L. Huang, H. Tang, X.L. Wang, J.P. Tu, Three-dimensional astrocyte-network Ni–P–O compound with superior electrocatalytic activity and stability for methanol oxidation in alkaline environments, J. Mater. Chem. A. 3 (2015) 4669.

[34] G. Socrates, Infrared and Raman Characteristic Group Frequencies: Tables and Charts, third ed., Wiley, 2001, p. 95.

[35] S. Fernandez, J.L. Mesa, J.L. Pizarro, L. Lezama, M.I. Arriortua, T. Rojo, Two new three-dimensional vanadium(III) and iron(III) phosphites templated by ethylenediamine: $(C_2H_{10}N_2)_{0.5}[M(HPO_3)_2]$. Ab initio structure determination, spectroscopic, and magnetic properties, Chem. Mater. 14 (2002) 2300–2307.

[36] S. Fernandez, J.L. Pizzaro, J.L. Mesa, L. Lezama, M.I. Arriortua, T. Rojo, Hydrothermal synthesis of a new layered inorganic–organic hybrid cobalt(II) phosphite: $(C_2H_{10}N_2)[Co_3(HPO_3)_4]$ Crystal structure and spectroscopic and magnetic properties, Int. J. Inorg. Mater. 3 (2001) 331–336.

[37] D. de Wall, C. Hunter, Vibrational spectra of solid solution of cadmium and calcium pyrophosphate, Mater. Res. Bull. 29 (11) (1994) 1129–1135.

[38] M. Tsuboi, Vibrational spectra of phosphite and hypophosphite anions, and the characteristic frequencies of PO_3^- and PO_2^- groups, J. Am. Chem. Soc. 79 (6) (1957) 1351–1354.

[39] L. Trotochaud, S.L. Young, J.K. Ranney, S.W. Boettcher, Nickel–iron oxyhydroxide oxygen-evolution electrocatalysts: the role of intentional and incidental iron incorporation, J. Am. Chem. Soc. 136 (2014) 6744–6753.

[40] P.W. Menezes, A. Indra, C. Das, C. Walter, C. Gobel, V. Gutkin, D. Schmeiber, M. Driess, Uncovering the nature of active species of nickel phosphide catalysts in high-performance electrochemical overall water splitting, ACS Catal. 7 (2017) 103–109.

[41] I. Sebarchievici, B.-O. Taranu, S.F. Rus, P. Vlazan, M. Poienar, P. Sfirloaga, Electro-oxidation of ascorbic acid on perovskite-modified electrodes, in: Tünde Alapi, István Ilisz (Eds.), Proceedings of the 25th International Symposium on Analytical and Environmental Problems, vols. 273–275, 7-8 October 2019, ISBN 978-963-306-702-4. Szeged, Hungary.

[42] M. Kolbacha, S. Fiechter, R. van de Krol, P. Bogdanoff, Evaluation of electrodeposited α-Mn_2O_3 as a catalyst for the oxygen evolution reaction, Catal. Today 290 (2017) 2–9.

[43] I. Sebarchievici, B.O. Taranu, M. Birdeanu, S.F. Rus, E. Fagadar-Cosma, Electrocatalytic behaviour and application of manganeseporphyrin/gold nanoparticle- surface modified glassy carbon electrodes, Appl. Surf. Sci. 390 (2016) 131–140.

[44] B. Jansi Rani, N. Dhivya, G. Ravi, S.S. Zance, R. Yuvakkumar, S.I. Hong, Electrochemical performance of β-nis@Ni$(OH)_2$ nanocomposite for water splitting applications, ACS Omega 4 (2019) 10302–10310.

[45] Y. Guo, L. Gan, C. Shang, E. Wang, J. Wang, A cake-style CoS_2@MoS_2/RGO hybrid catalyst for efficient hydrogen evolution, Adv. Funct. Mater. 27 (2017) 1602699.

[46] Q. Li, S. Tang, Z. Tang, Q. Zhang, W. Yang, Microwave-assisted synthesis of $FeCoS_2$/XC-72 for oxygen evolution reaction, Solid State Sci. 96 (2019) 105968.

[47] R. Liu, Z. Ji, J. Wang, J. Zhang, Mesocrystalline TiO_2/sepiolite composites for the effective degradation of methyl orange and methylene blue, Front. Mater. Sci. 12 (2018) 292–303.

[48] C. Liu, H. Ma, M. Yuan, Z. Yu, J. Li, K. Shi, Z. Liang, Y. Yang, T. Zhu, G. Sun, H. Li, S. Ma, $(NiFe)S_2$ nanoparticles grown on graphene as an efficient electrocatalyst for oxygen evolution reaction, Electrochim. Acta 286 (2018) 195–204.

[49] V. Mani, S. Anantharaj, S. Mishra, N. Kalaiselvi, S. Kundu, Iron hydroxyphosphate and Sn-incorporated iron hydroxyphosphate: efficient and stable electrocatalysts for oxygen evolution reaction, Catal. Sci. Technol. 7 (2017) 5092–5104.

[50] Y. Zhao, S. Chen, B. Sun, D. Su, X. Huang, H. Liu, Y. Yan, K. Sun, G. Wang, Graphene-Co_3O_4 nanocomposite as electrocatalyst with high performance for oxygen evolution reaction, Sci. Rep. 5 (2015) 7629.

[51] H. Xu, W. Zhang, J. Zhang, Z. Wu, T. Sheng, F. Gao, An Fe-doped $Co_{11}(HPO_3)_8(OH)_6$ nanosheets array for high-performance water electrolysis, Electrochim. Acta 334 (2020) 135616.

[52] Y.-H. Chiu, T.-F. Mark Chang, C.-Y. Chen, M. Sone, Y.-J. Hsu, Mechanistic insights into photodegradation of organic dyes using heterostructure photocatalysts, Catalysts 9 (2019) 430.

[53] C.H. Nguyen, C.C. Fu, R.S. Juang, Degradation of methylene blue and methyl orange by palladium-doped TiO_2 photocatalysis for water reuse: efficiency and degradation pathways, J. Clean. Prod. 202 (2018) 413–427.

[54] L.V. Trandafilovic, D.J. Jovanovic, X. Zhang, S. Ptasinska, M.D. Dramicanin, Enhanced photocatalytic degradation of methylene blue and methylorange by ZnO:Eu nanoparticles, Appl. Catal. B Environ. 203 (2017) 740–752.

[55] B. Rodríguez-Cabo, I. Rodríguez-Palmeiro, R. Corchero, R. Rodil, E. Rodil, A. Arce, A. Soto, Photocatalytic degradation of methyl orange, methylene blue and rhodamine B with AgCl nanocatalyst synthesized from its bulk material in the ionic liquid $[P_{6\ 6\ 6\ 14}]$Cl. Water, Sci. Technol. 75 (2017) 128–140.

[56] A. Ajmal, I. Majeed, R.N. Malik, H. Idriss, M.A. Nadeem, Principles and mechanisms of photocatalytic dye degradation on TiO_2 based photocatalysts: a comparative overview, RSC Adv. 4 (2014) 37003–37026.

[57] A. Houas, H. Lachheb, M. Ksibi, E. Elalou, C. Guillard, J.M. Herrmann, Photocatalytic degradation pathway of methylene blue in water, Appl. Catal. B Environ. 31 (2001) 145–157.

[58] H.A. Kiwaan, T.M. Atwee, E.A. Azab, A.A. El-Bindary, Photocatalytic degradation of organic dyes in the presence of nanostructured titanium dioxide, J. Mol. Struct. 1200 (2020) 127115.

[60] E.L. Simmons, Diffuse reflectance spectroscopy: a comparison of the theories, Appl. Optic. 14 (1975) 1380.

[61] H. Anwer, A. Mahmood, J. Lee, K.H. Kim, J.W. Park, A.C.K. Yip, Photocatalysts for degradation of dyes in industrial effluents: opportunities and challenges, Nano Res. 12 (2019) 955–972.

[62] R.C. Che, L.-M. Peng, W.Z. Zhou, Synthesis and characterization of crystalline microporous cobalt phosphite nanowires, Appl. Phys. Lett. 87 (2005) 173122.

[63] L. Brus, Quantum crystallites and nonlinear optics, Appl. Phys. A 53 (1991) 465–474.

[64] F. Consadori, R.F. Frindt, Crystal size effects on the exciton absorption spectrum of WSe_2, Phys. Rev. B 2 (1970) 4893.